Journal of Manufacturing Processes 120 (2024) 1231–1240

Contents lists available at ScienceDirect

Journal of Manufacturing Processes

journal homepage: www.elsevier.com/locate/manpro

Understanding oblique deposition in aerosol jet printing for conformal electronics fabrication

Jeremy D. Rurup, Ethan B. Secor *

Department of Mechanical Engineering, Iowa State University, Ames, IA 50011, USA

ARTICLE INFO

Keywords:
Additive manufacturing
Printed electronics
Hybrid electronics
Digital manufacturing

ABSTRACT

Aerosol jet printing is a compelling additive manufacturing technology to enable direct patterning of electronic devices onto complex 3D surfaces. While aerosol jet printing can support deposition in an oblique configuration (with the nozzle misaligned from the surface normal), the altered deposition physics associated with this have not been examined. We address this gap from a fundamental perspective, coupling experiments and numerical simulation to understand the effect of asymmetry in the oblique jet, which sweeps small aerosol droplets downhill on tilted substrates. Modeling results of an oblique aerosol jet show that, although larger droplets are relatively unaffected due to their greater inertia, the altered impaction of smaller droplets results in an asymmetric cross-sectional profile and increased line width, which is sensitive to both the nozzle-surface orientation and offset distance. To complement the numerical simulations, silver traces are printed with varying gas flow rates, nozzle standoff distance, and nozzle orientation. Asymmetry, line width, and resistance increase with tilt angle, an effect reduced at higher flow rates and closer nozzle positioning, corroborating the numerical model. Finally, a printhead mounted on a 6-axis robotic arm was used to conformally print onto a complex 3D surface, showing improved flexibility in process design and highlighting the challenging geometries that can be accommodated when the fundamental mechanisms of oblique aerosol printing are considered.

1. Introduction

A key advantage of additive manufacturing (AM) methods is the ability to fabricate complex parts with geometry too difficult or expensive to produce with conventional techniques. Engineers in automotive, aerospace, medical, and other industrial sectors have applied both polymer and metal AM to increase customizability, shorten development cycle timelines, reduce size, weight, and power characteristics, and simplify complex assemblies, to name a few [1,2]. While significant efforts have focused on structural components, emerging methods suitable for functional materials are enabling more geometrically complex electronic devices. Conductive filaments have been available for fused deposition modeling for years, allowing conductive traces to be printed directly within the structure of complex, 3D components, albeit with limited electrical performance [3,4]. Thin film printed electronics techniques including inkjet, gravure, and screen printing have been used in tandem with silicon integrated circuits to fabricate flexible and hybrid electronic devices on flat substrates, with proposed applications in wearable medical devices, structural health monitoring, and industrial and environmental sensors [5–7]. These flexible devices have even been bonded onto 3D structures with shallow or 1D curvature.

Aerosol jet printing (AJP), on the other hand, is capable of directly printing on topographically complex surfaces, enabling true conformal electronics fabrication [8]. AJP is suitable for a wide variety of materials, and exhibits a minimum feature size range of 10–20 μm with a large nozzle-substrate offset distance of 1–5 mm. On flat, 2D substrates, AJP has been employed to fabricate devices for communication [9–11], sensing [12–14], logic [15,16], and energy storage [17,18], among other applications. AJP has attracted significant interest for electronics packaging, with its large nozzle standoff enabling it to print 2.5D features and contour nonuniform surfaces [19,20]. With regard to conformal electronics printing, AJP has been demonstrated for ear mold circuitry [21], thermoelectric devices [22], capacitive sensors [23], RF devices [24], and structural drone components [25], to name a few. The substrates for several of these examples were printed via additive methods, including stereolithography, fused deposition modeling, and selective laser sintering.

Despite its ostensible suitability for conformal electronics printing,

* Corresponding author.
E-mail address: esecor@iastate.edu (E.B. Secor).

https://doi.org/10.1016/j.jmapro.2024.05.004
Received 17 October 2023; Received in revised form 12 February 2024; Accepted 1 May 2024
Available online 15 May 2024

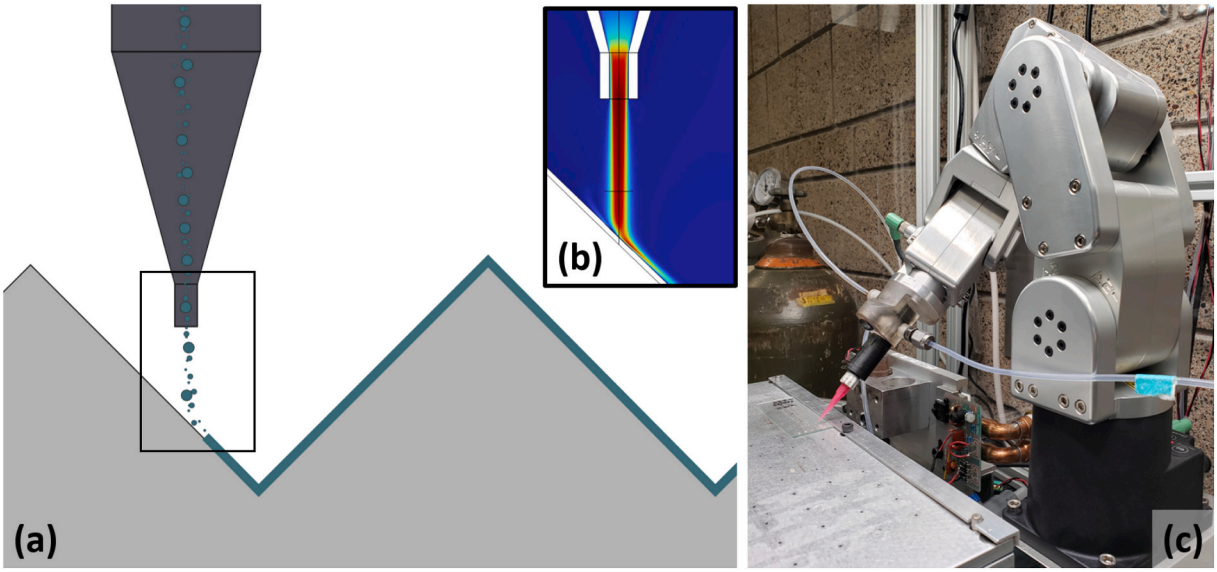

Fig. 1. (a) Oblique deposition occurring during aerosol jet printing on a substrate surface contoured as a triangular wave pattern. (b) Asymmetry in the simulated velocity field of gas impinging on a 45° tilted substrate. (c) Custom aerosol jet printer employing an articulated 6-axis robot arm, shown printing 45° off-normal from the substrate.

Table 1
Default values and ranges for simulation parameters.

Parameter	Default value	Range
Nozzle diameter	200 μm	100–300 μm
Carrier gas flow rate	10 sccm	6–16 sccm
Sheath gas flow rate	50 sccm	10–80 sccm
Standoff distance	1.5 mm	0.5–5.0 mm
Tilt angle	26.6°	0–60°
Droplet size	NA	0.5–5.0 μm

the underlying process science of AJP in this modality has not been previously explored. In the above listed conformal AJP examples, many would have been printed at least in part in an oblique configuration. Such a case, in which the jet is not aligned normal (perpendicular) to the surface, is therefore of particular interest. For conformal printing with a 3-axis printer, this configuration is unavoidable; for printing with a 5-axis machine (e.g., Optomec AJ 5X trunnion system), tolerance for oblique deposition can ease kinematic constraints and broaden the available surface geometries amenable to printing. As an example, for the triangular waveform geometry shown in Fig. 1a, there are three potential strategies for toolpath planning. First, and most simplistic, the motion system could be programmed to stay at a fixed *Z*-position and fixed *Z*-axis tilt with respect to the substrate. This would result in a varying nozzle-substrate offset distance, as well as oblique deposition. Second, the *Z*-position could be varied to match the substrate geometry, retaining a constant nozzle standoff distance, while fixing the *Z*-axis orientation to vertical – again resulting in oblique deposition. Third, if printer hardware allows, both the *Z*-position and *Z*-axis tilt could be varied to retain constant nozzle standoff distance and a surface-normal orientation, with challenges arising at sharp corners where some regions may be occluded or not possible within kinematic constraints of the motion system.

To rationally approach this type of complex conformal printing application, a more holistic understanding of oblique deposition in an aerosol jet is required beyond the current understanding of 2D, flat horizontal deposition. To first order, AJP is often considered as a line-of-sight printing method. However, as illustrated by numerical simulations (Fig. 1b), oblique impaction eliminates symmetry in the gas velocity field. This affects the trajectories of aerosol droplets within the jet, altering where, and even whether, they impinge on the surface. A more complete fundamental understanding of this phenomenon is critical to apply AJP in more demanding geometries. This could include constrained interior curvature where surface-normal printhead orientation is impossible, deposition on structured surfaces where rapid changes to tool orientation are impractical, and abrupt changes in surface orientation for which collision avoidance considerations and kinematic constraints prevent surface-normal deposition, among others. Conformal printing of electronics is among the most distinguishing capabilities for AJP, and a fundamental understanding of the physics that define its limitations is critical to further advancing this versatile technology in new application domains.

To study the oblique aerosol deposition phenomenon and better understand limitations and key parameters governing oblique deposition in AJP, we applied a combination of numerical modeling and experiments. Numerical modeling allows precise variation of droplet size, tilt angle, standoff distance, and gas flow parameters, and supports evaluation of the deposition width and profile. To corroborate insight from numerical models, a series of prints was performed on a custom aerosol jet printer employing a 6-axis robot arm as the primary motion system (Fig. 1c). From prints conducted at multiple tilt angles, flow rates, and nozzle offset distances, the cross-sectional profile, line width, and conductance were measured. From this combination of experimental and numerical results, this work intends to establish a more comprehensive foundation to understand the physics of oblique deposition in AJP, enabling broad improvements in machine design, process parameter optimization, materials development, and toolpath planning for conformal electronics.

2. Theory and simulation setup

Aerosol droplet impaction is governed by the motion of particles within the flow field of an impinging gas jet. In this multiphase flow, both the flow field of the impinging jet and the liquid droplet motion need to be solved to characterize oblique impaction in AJP. Computational fluid dynamics (CFD) software is used to solve the velocity field of the impinging jet, as described below. Important parameters describing the gas flow include the nozzle exit diameter, gas velocity, and impinging surface geometry. The behavior of a particle in an impinging jet is governed primarily by its inertia, described in dimensionless form by the Stokes number (St) [26].

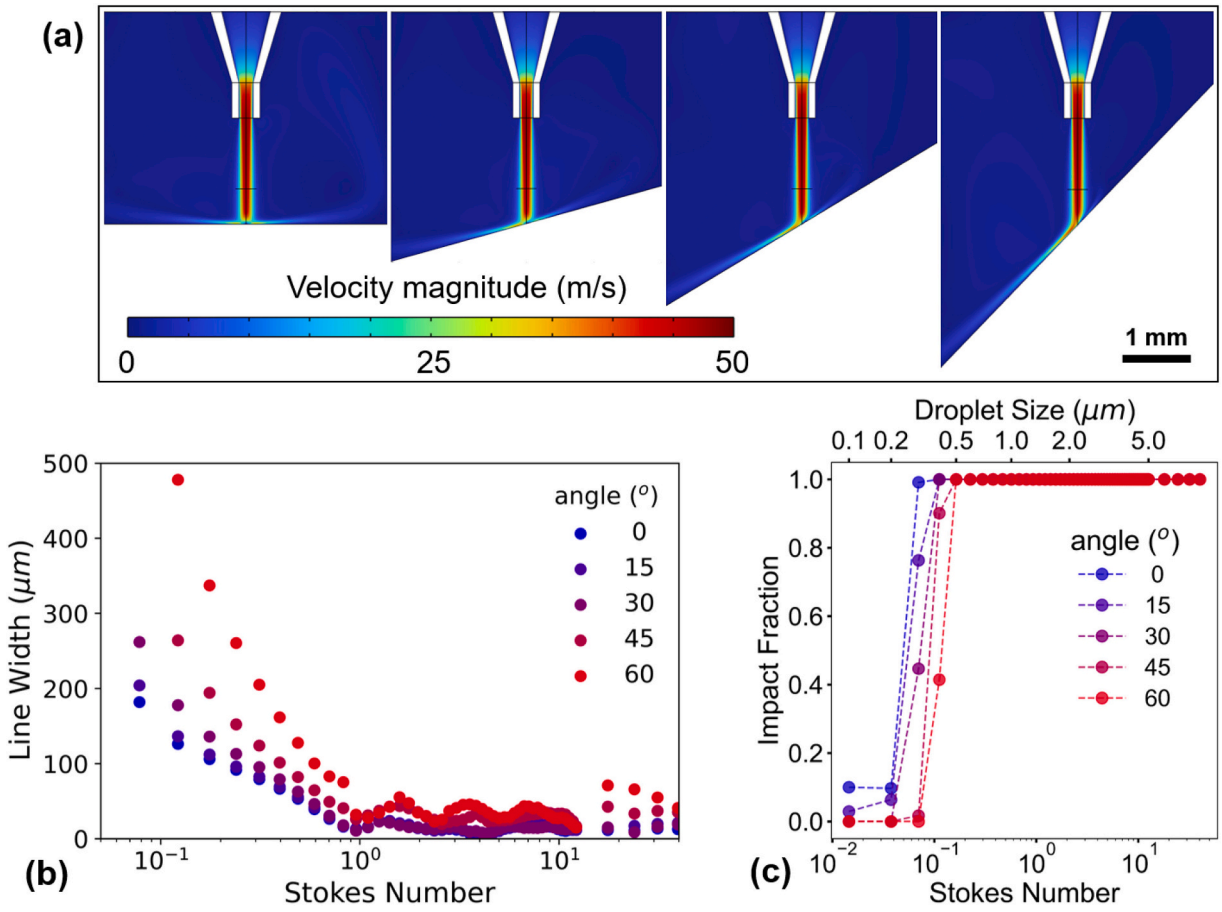

Fig. 2. (a) Simulated gas velocity fields for substrates tilted at 0° (surface normal), 15°, 30°, and 45°, showing asymmetry near the substrate surface. (b) Line width and (c) impact fraction as a function of Stokes number (droplet size), with line width generally increasing and impaction efficiency generally decreasing with increasing substrate tilt angle.

$$St = \frac{\rho_p d_p^2 C_c u}{18 \mu D_n} \quad (1)$$

Here, ρ_p is the droplet density (kg m^{-3}), d_p is the droplet diameter (m), C_c is a slip correction factor, u is the average gas velocity (m s^{-1}), μ is the gas viscosity (kg m^{-1} s^{-1}), and D_n is a characteristic length scale, expressed here as the nozzle diameter (m). The Stokes number arises from nondimensionalization of Stokes drag force, which describes the tendency of suspended particles to follow the fluid streamlines. Deviation of the particle velocity from that of the surrounding fluid arises from inertia; conceptually, in the impinging jet a droplet of larger diameter will exhibit less change in velocity and maintain its trajectory in line with the nozzle exit, while a smaller droplet will be more susceptible to drag from the gas flow field and be swept further away from the jet axis. This effect can be seen visually in many aerosol jet prints in the form of overspray. If sufficiently small, a droplet may not separate from the gas phase and be swept off into the atmosphere. Stokes drag force is not the only physics at play, with lift forces also having a role, but because it is relevant for the line edge behavior (e.g., resolution and overspray) under a wide range of printing conditions, the Stokes number bears particular consideration during analysis of the process.

By itself, the Stokes number acts only as a qualitative metric for determining the impaction characteristics of a particle. For more precise study, a numerical model was set up using COMSOL® Multiphysics (Supplemental Information, Section SI 1). While numerical modeling of standard AJP has been well established [27–31], oblique deposition significantly alters the flow field and thus the deposition physics. The gas flow field is first modeled as weakly compressible flow, then Lagrangian particles are released and tracked under the influence of drag force, lift force, and gravity. Two droplet release features are the focus of analysis: a ring of droplets released at the periphery of the aerosol stream, to visualize the greatest extent of the deposit; and a line of particles released along the nozzle center line, aligned with the surface tilt, to reflect the distribution of droplets within the aerosol stream. The final positions of droplets corresponding to the ring release feature are projected onto the tilted substrate and fit with an ellipse to get a value for line width (Fig. S1). For the slot release feature, the uniformly distributed droplets are weighted by the flow velocity in the carrier gas (i.e., assuming uniform droplet density within the carrier gas upstream) to estimate the fraction of droplets that impinge the surface and the 1D profile of the released droplets on the surface (note: this is not a simulated line cross section directly but conveys similar information).

With a modeling capability established, a series of numerical experiments was designed to investigate different features of the deposition process. Two broad classes of variables were considered: the geometrical configuration, encompassing the tilt angle and standoff distance (vertical distance from nozzle exit to surface), and the flow parameters (carrier and sheath gas flow rates, nozzle diameter). For a typical simulation, droplets with diameters from 0.5 to 5.0 μm were considered. The baseline parameters for numerical modeling studies (default settings when isolating other variables) are listed in Table 1.

3. Materials and methods

3.1. Inks and materials

The ink used in all experiments was UTD-Ag40X from UT Dots, Inc.,

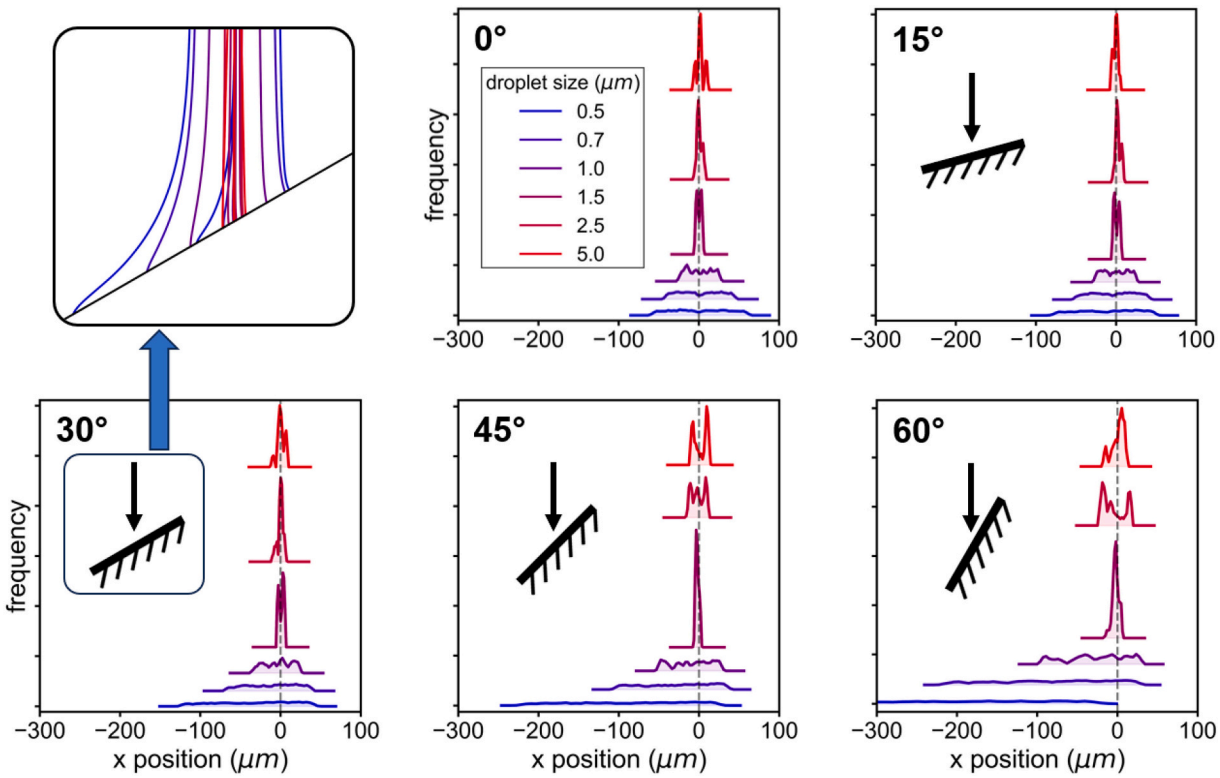

Fig. 3. Comparison of cross-sectional profiles for droplets of various sizes on substrates tilted at 0° (surface normal), 15°, 30°, 45°, and 60° as predicted by the numerical simulations, along with trajectories of individual droplets in the 30° case.

nominally a dispersion of 40 % silver nanoparticles by weight in xylenes. The base ink was modified by adding terpineol and additional xylenes, resulting in a mixture of 2:7:1 v/v UTD-Ag40X/xylenes/terpineol. The primary reason for ink modification is to modulate the evaporation characteristics, based on the higher boiling point of the terpineol cosolvent, as discussed in detail elsewhere [32]. Unless otherwise noted, glass microscope slides were used as the substrate to provide a smooth, flat baseline for measurements. Prior to characterization, the silver nanoparticle prints were sintered on a hotplate at 250 °C for 1 h. For demonstration of printing on a 3D surface, stereolithography resin (Formlabs clear resin) was used for surface preparation.

3.2. Printing hardware

A custom aerosol jet printer was built employing a Mecademic Meca500 6-axis robot arm as the motion system, which accepts Cartesian motion commands. Software was written to integrate control of the robot arm and other components of the printing system. This included mass flow controllers from Alicat and an ultrasonic atomizer containing a 1.65 MHz piezoelectric nebulizer from American Piezo. Custom printhead components were printed via stereolithography and mounted on the robotic arm motion system to enable effective AJP. Standard pneumatic fittings (Luer lock and Swagelok) and tubing connected the ultrasonic atomizer to the printhead.

3.3. Characterization methods

A Zygo NewView™ 9000 optical profilometer was used to collect both the cross-sectional area and line width measurements. A post-processing script averaged area and width measurements across the 1.7 mm span of the 2D profilometry data to compute a reliable output. A Keithly 2450 source meter coupled with an electrical probe station was used to collect electrical measurements in an in-line 4-point probe configuration (Fig. S3).

4. Results and discussion

While many applications in AJP allow the nozzle to be maintained orthogonal to the surface, this is not possible or desirable for all substrates. Because many such prints will have strict tolerances on feature size or resistance, the primary objective of this work is to examine the effects of oblique deposition on these process metrics. Data from both the multiphysics simulation and physical prints conducted with the robot printer are examined to provide insight on general outcomes and criteria for oblique deposition.

4.1. Effects of droplet inertia

Aerosol transported from the ink cartridge to the nozzle is polydisperse [33], resulting in a wide range of St even when the carrier and sheath gas flow rates are held constant. The numerical model yielded a unique opportunity to examine impaction properties for precise droplet sizes, retaining information otherwise lost in a physical print. For printing with a nozzle diameter of 200 μm, nozzle surface offset of 1.5 mm, and carrier and sheath gas flow rates of 10 sccm and 50 sccm, respectively, the simulation first solved for the gas flow field, followed by the trajectory of droplets released into this steady state gas flow field. This process was repeated at tilt angles of 0° (normal to the surface), 15°, 30°, 45°, and 60° offset from surface normal. Several of the gas flow fields are shown in Fig. 2a, exhibiting increased asymmetry at higher tilt angles. For a given droplet size, variations in impaction properties are a result of this asymmetry in the flow field.

The model reveals that the expected line widths (Fig. 2b) and impact fractions (Fig. 2c) for droplets larger than approximately 1 μm are relatively unaffected by oblique deposition at this flow rate. Even when pushed to a fairly extreme angle of 60°, the effects are minimal for both line width and impact fraction. On the other hand, the smaller droplets are more adversely affected, with line widths increasing by well over 100 μm for the smallest droplets. For all substrate tilt angles, the

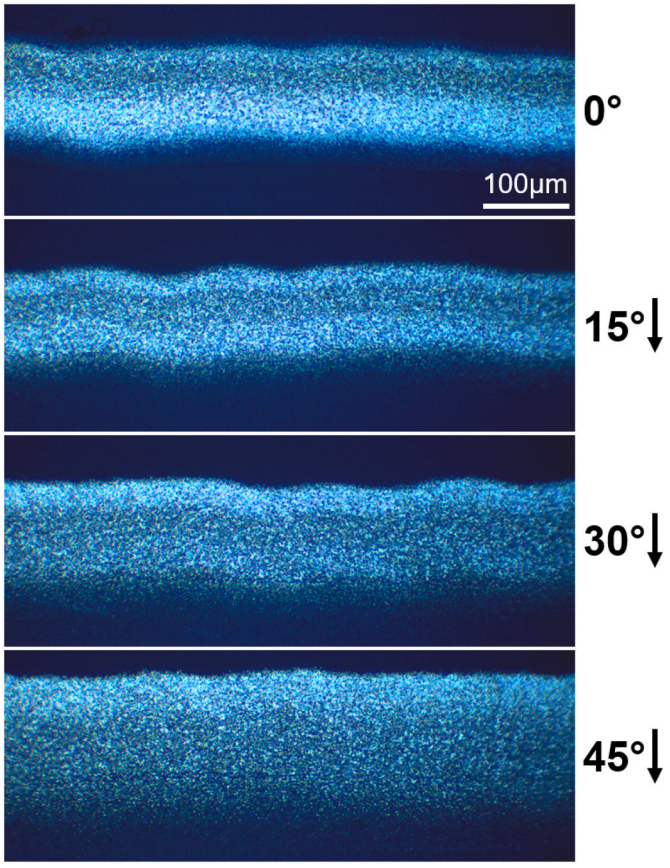

Fig. 4. Microscope images of the 15 sccm dataset, with line width and asymmetry increasing as nozzle-substrate angle increases from 0° (surface normal) to 45°.

impaction probability was near 1 for larger droplets, then decayed abruptly to near 0 below a certain threshold size. Increasing the tilt angle increased this threshold droplet size, shifting the curve to the right.

The plots shown in Fig. 3 depict the anticipated impact locations of droplets in the aerosol stream at multiple tilt angles, in terms of frequency at a given position, revealing information related to the cross-sectional profile. To obtain these results in COMSOL®, first the gas flow field was solved, then a line of droplets was released along the nozzle midline, as discussed in the preceding section on Theory and Simulation Setup and in the SI (Section SI 1, Fig. S1). Because a true aerosol stream will be polydisperse, this does not predict a true cross-sectional profile, but it does indicate how droplets of various sizes are affected by the asymmetry in the gas flow field. As with line width and impact fraction, larger droplets greater than 1 μm in diameter are relatively unaffected. However, for droplets this size and smaller, a noticeable shift of the deposition midpoint occurred, in addition to an increase in estimated line width. Because of this center-shift, the line widths shown in Fig. 2b may actually be under-estimates for true, polydisperse deposition, particularly at the more extreme angles.

For an experimental comparison to the simulation results, samples were printed at 15°, 30°, and 45° offset from normal, with an additional control case at surface normal (0°). On the 6-axis robot arm printer, this was accomplished by tilting the printhead, leaving the substrate in a horizontal plane, as depicted in Fig. 1c. For aerosol droplets on the scale of 1–5 μm, aerodynamic forces dominate, with the effects of gravity being negligible [26]. At each angle, a 10 mm long, single-layer line was printed at a constant speed of 2 mm/s. In an actual AJP process, droplet size cannot be explicitly controlled and discretized. To achieve an indirect variation in droplet inertia, the carrier and sheath gas flow rates were instead altered. Specifically, a total of three prints were completed at carrier gas flow rates of 12, 15, and 18 sccm, with a focusing ratio (sheath-to-carrier gas flow rate ratio) of 5 for each. After printing and sintering, the line width, cross-sectional area, and conductance were measured.

In microscope images of the 15 sccm dataset (Fig. 4), the evident increase in line width is accompanied by visual asymmetries as the tilt angle increases. Particularly in the 30° and 45° lines, the line is more diffuse on the lower edge, suggesting a more pronounced region of overspray. In Fig. 5a, the cross-sectional profiles of these lines are examined in more detail. In agreement with the images, the cross-section becomes more asymmetric as the tilt angle increases. This result is consistent with the simulated model, in which smaller droplets are deposited further down the slope from the axis of symmetry, while the line edge on the uphill side of the jet axis has close spacing between the maximum extent of different droplet sizes. As a result, the lines broaden with increasing tilt angle at all carrier gas flow rates, as shown in Fig. 5b. While an increase in line width would be expected due to projection effects even with perfect line of sight patterning, the increase in measured line widths exceeds that expected from a simple trigonometric projection, as shown in Fig. S4. This further supports the assertion that the asymmetric flow field from the oblique geometry has nontrivial effects on droplet trajectories, aligning with the simulation result showing smaller droplets, those more prone to cause overspray, pushed further down the slope from the jet axis to cause asymmetry in the cross-sectional profile.

Furthermore, a decrease in conductance is observed as the tilt angle increases for all three carrier flow rates. This correlates well with simulation results and suggests that the impaction efficiency of the printing process can decrease as the tilt angle increases. Interestingly, resistivity also increased substantially in the 12 and 15 sccm prints at 30° and 45°, prints for which significant overspray was present. While the volume of this deposited material was measurable via profilometry, not all of it appeared to be electrically continuous, leading to the increase in resistivity. Based on the numerical model, oblique impaction can more effectively segregate different droplet sizes. For this particular silver nanoparticle ink, an especially dry print with smaller droplet sizes could also lead to a more porous microstructure following sintering.

While the exact outcomes of oblique deposition will depend on both the printer and ink composition, these results provide key insight into the underlying physics and will support more rational and science-based process development. Oblique deposition may compound with other factors affecting line morphology, such as feed rate, sheath gas flow rate, and ink viscosity and surface tension. In an ultrasonic atomizer, ink surface tension contributes to droplet size, which affects St at impaction and viscosity affects the volume of liquid ink aerosolized [34,35]. Ink formulation also dictates aerosol drying during transport, which is why many inks contain some amount of low volatility cosolvent, such as the terpineol employed in this modified ink [36]. Reducing the print speed or increasing carrier flow rate can incur additional spreading of liquid phase ink on the substrate surface, resulting from more material deposited per unit length [37]. If liquid is deposited on the surface, its behavior will be dictated primarily by viscosity and surface tension, and higher carrier and sheath flow rates will impart additional shearing on the liquid surface, which would be asymmetric in an oblique configuration.

Regardless, when printing with the nozzle oblique to the substrate, asymmetry in the cross-sectional profile can be expected due to the Stokes drag force on droplets in the asymmetric gas flow field caused by oblique deposition. This physical process occurs prior to deposition on the substrate and will generally cause an increase in line width, as well as a decrease in the volume of material deposited during oblique deposition. These general effects are more clear when considering many-layered prints targeting high aspect ratio deposition, in which the previously-deposited material can influence the aerosol flow field alongside the geometry of the substrate alone (Fig. S5). Other

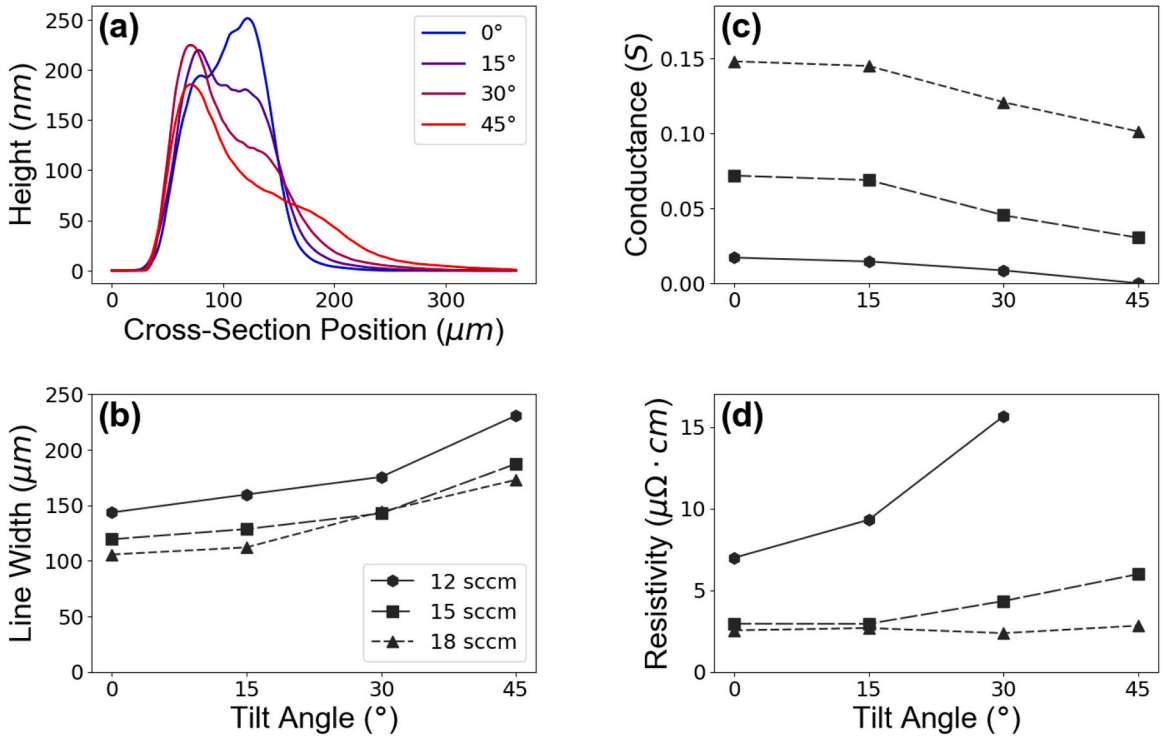

Fig. 5. (a) Cross-sectional profiles for the 15 sccm prints, showing increased asymmetry as the tilt angle increases. (b) Line width, (c) conductance, and (d) resistivity as a function of tilt angle for multiple carrier gas flow rates.

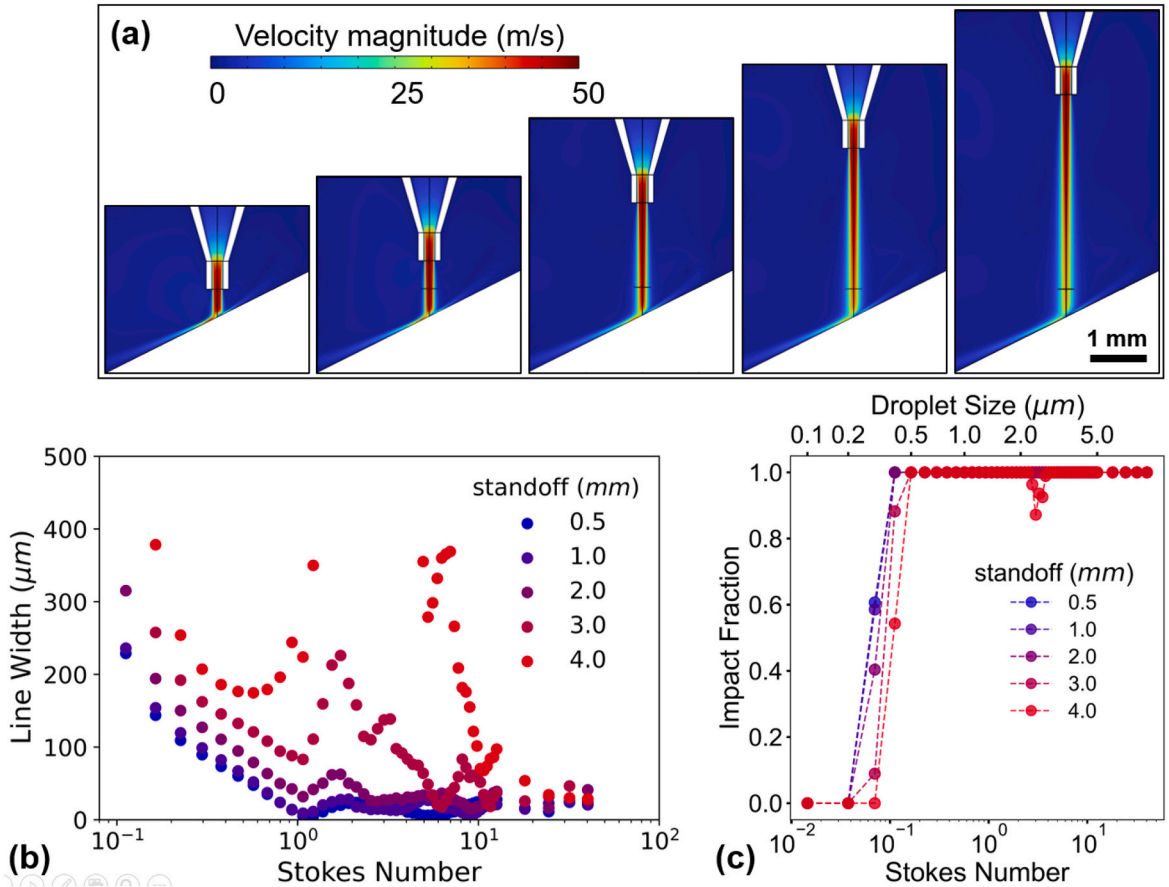

Fig. 6. (a) Simulated gas velocity fields for nozzle offset distances of 0.5, 1, 2, 3, and 4 mm (left to right) with the substrate tilted at 30°, showing a decrease in velocity in the free jet region for larger nozzle standoff distances. (b) Line width and (c) impact fraction as a function of Stokes number (droplet size) for several nozzle standoff distances, each 30° oblique to the surface normal.

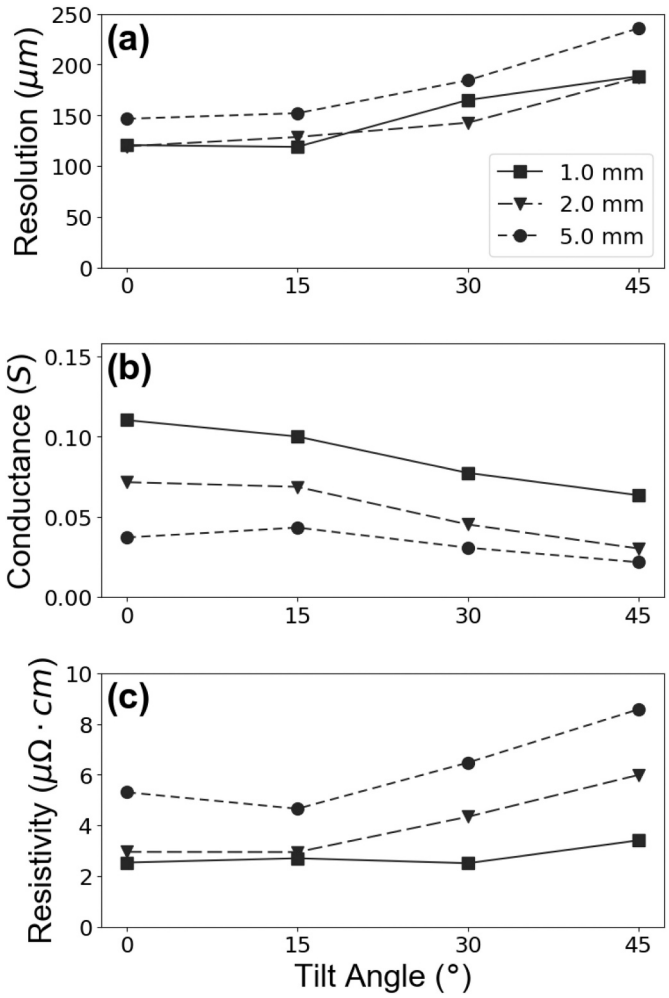

Fig. 7. (a) Line width, (b) conductance, and (c) resistivity as a function of tilt angle for multiple nozzle offset distances.

morphological defects occurring from upstream effects, such as discontinuities or excessive line edge roughness, will follow suit. To mitigate these negatives, flow rates may be adjusted to increase droplet inertia and minimize downsides associated with oblique impaction.

4.2. Varying nozzle offset distance

One of AJP's most desirable aspects for conformal electronics printing is its noncontact operation with large nozzle-to-surface offset distance, making it relatively tolerant to dimensional variation or imperfect fixturing of the substrate. However, the effect of offset distance within the broad range considered suitable remains underexplored. With regard to upper limits on standoff distance, Feng explored the laminar breakdown length of aerosol exiting the nozzle [38], although this generally exceeded the more typical operational standoff distance of 1–5 mm. In this section, nozzle standoff is more rigorously explored in the context of oblique deposition in AJP, via both numerical simulations and experiments.

Using the same default parameters as previously, numerical simulations were performed varying the nozzle-surface standoff distance. The flow fields (velocity magnitude) associated with different standoff distances from 0.5 to 4 mm are shown in Fig. 6a, showing notable differences in the jet velocity. After reaching peak velocity in the narrowest portion of the nozzle, the gas slows as the jet expands laterally after exiting the nozzle. As the standoff distance increases, the jet velocity decays more before entering the near-wall zone, nominally reducing the inertia of the aerosol droplets. For the smallest droplets, below approximately 1 μm in diameter, this has the expected effect – increasing line width and increasing the threshold diameter for successful impaction. With the larger droplets, there is little difference between closer standoff distances (0.5–2 mm). However, with the nozzle offset 3 or 4 mm from the surface, the velocity of the jet drops below the droplet velocity. The suspended droplets, exhibiting a higher velocity than the surrounding gas, then experience a lift force directed away from the jet axis. While prior studies have discussed the effect of lift forces as a focusing mechanism within a slowly converging capillary of an aerosol jet nozzle [29,39,40], these results suggest the significance of these forces in the stagnating jet as a mechanism of defocusing. This effect causes the large spike in line width for St ~1–10 for nozzle offsets of 3 and 4 mm. In general, the models confirmed that varying the nozzle offset distance affects the gas velocity field, which in turn can alter impaction properties.

Experimentally, 10 mm long lines were printed with a constant speed of 2 mm/s at 0° (surface normal), 15°, 30°, and 45° by tilting the robot arm with respect to the substrate, as in the previous section. Prints were performed with nozzle offset distances of 1, 2, and 5 mm, with the carrier flow rate set to 15 sccm at a focusing ratio of 5 for all three sets of prints. Much like the prints in the previous section, the line width increases with tilt angle (Fig. 7, Fig. S6). However, the measured line widths for the 1 mm and 2 mm nozzle offsets were generally very similar, while the lines printed at the 5 mm offset are on the order of 25–30 μm wider. With a greater nozzle offset, the jet slows more as it approaches the substrate, meaning the droplets may have lower inertia entering the near-wall region before impaction or before being swept aside.

Based on the measurement of electrical conductance, increasing the nozzle offset distance appears to substantially reduce impaction efficiency at this flow rate. This trend is attributed to the changes described above based on the simulations. For the parameter ranges evaluated here, the nozzle offset distance had a stronger effect on the measured conductance, and therefore impaction efficiency, than the tilt angle. The conductance continues to decrease as tilt angle increases for all three nozzle offset distances. Likewise, the resistivity trends upwards in all three sets of prints, suggesting regions of overspray that contributed to the cross-sectional area measurement but were not electrically continuous. Increasing the nozzle offset distance exacerbated this effect. While all three nozzle offset distances produced successful prints, keeping the nozzle closer to the substrate surface – between 1 and 2 mm – generally led to higher quality prints, resulting in resolution and resistivity at an apparent minimum. Given the popular conception of AJP as being largely invariant to standoff distance within a broad range, often cited as 1–5 mm, these results are particularly noteworthy for imposing soft constraints to oblique deposition.

4.3. Application to conformal electronics printing

The fundamental knowledge and capability to rationally design for oblique deposition enables greater versatility in conformal electronics printing. On a substrate with surface curvature or otherwise nonplanar features, 3-axis aerosol jet printers will be required to print in an oblique configuration. More complex 5-axis systems, as well as the 6-axis robot arm demonstrated in this work, have some capability to maintain orthogonality with the surface during printing operations. However, doing so in practice may not be feasible or desirable for all substrate geometries. While results in the previous sections show an orthogonal printing orientation to be ideal for impaction physics, they also reveal a substantial tolerance for oblique deposition, particularly if best practices for standoff distance and droplet inertia are maintained. Within a suitable subset of process parameters, efficient printing at tilt angles of up to 45° has been shown possible, with larger angles a potential target as well.

To validate the primary findings of this work, a substrate with angled

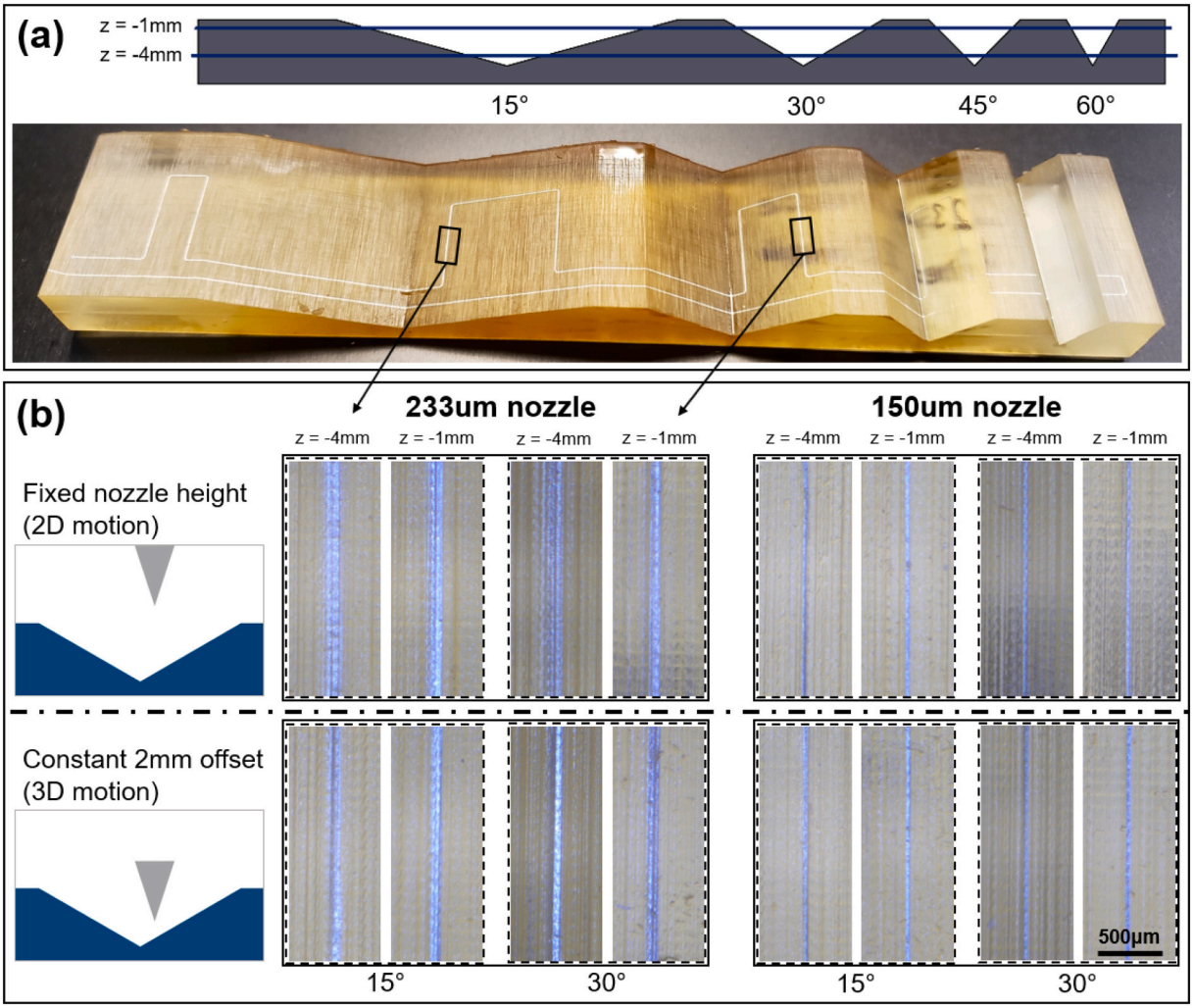

Fig. 8. (a) Ridged test surface with varying surface orientation and lines printed at different depth below the top surface. (b) Optical microscopy images for different line heights, surface angles, and nozzle diameters for each of the two motion strategies.

surfaces was fabricated by 3D printing. Two different motion planning approaches were used for aerosol jet printing of silver on these surfaces: maintaining the nozzle at a fixed z position (2-axis motion), and maintaining the nozzle at a fixed orientation but tracking the z position of the surface, always 2 mm off the surface (3-axis motion). For each condition, lines were printed 1 and 4 mm below the top substrate surface, bringing the total nozzle offsets for the fixed z position (2-axis motion) case to 3 mm and 6 mm, respectively. The printed lines were analyzed at angles of 15° and 30°, and the test was repeated with 233 and 150 μm nozzles at a carrier flow rate of 15 sccm. To further contrast the difference in droplet inertia, a focus ratio of 3 was used with the 233 μm nozzle and a focus ratio of 8 with the 150 μm nozzle. The test setup and results are shown in Fig. 8. For the 233 μm nozzle, there is little effect of standoff distance for the slightly tilted surface (15°) when the nozzle is held at a fixed z position, which aligns with the general notion that AJP is largely insensitive to standoff distance within a large range of ~1–5 mm. However, this same configuration with a 30° tilt results in a significant loss in line quality for the higher standoff distance of 6 mm. This change in line quality with standoff distance can be addressed by using 3-axis motion, with the printhead z position varied to maintain a constant standoff distance of 2 mm. When a smaller nozzle diameter of 150 μm and higher focus ratio is used to increase the droplet Stokes number, the effects of oblique deposition are significantly reduced even in the fixed z height (2-axis motion) case, in agreement with the experiments and model results above. For the fixed z height configuration, the printed line width increases from 40 μm at a surface normal (0°) orientation to 50 μm at 30° with a surface offset of 6 mm, while remaining ~40 μm for a surface offset of 3 mm (SI 6, Fig. S7). While still present, the increase in line width is more modest due to the increased inertia of the droplets.

To demonstrate this with a more complex pattern, a two-arm log-periodic spiral antenna pattern was printed on a corrugated disk. Near the center, the aerosol jet printed arms are about 150 μm in width, but widen to 1200 μm as the pattern extends radially, which is a feature of this antenna geometry to improve interaction with electromagnetic fields. The substrate can most easily be thought of as a triangular wave pattern repeated rotationally around a central axis, with the amplitude of the wave increasing away from the center. Each wave has a peak-to-peak height of 5.25 mm at the outside edge, as shown in Fig. 9a, and each slope was inclined 45° from horizontal. Planar toolpaths for the spiral pattern were generated with Slic3r, a standard slicing program for fused deposition modeling printers. Because of the large peak-to-peak height, printing at a fixed *Z*-height would have resulted in standoff distances greater than 5 mm, causing substantial variations in line width and deposition rate in different regions of the part. Therefore, a Python script was written to parse the G-code commands output by the slicing program, project toolpaths onto the 3D surface, and output a final set of commands in the native control language of the robot printer. This conformal toolpath enabled the nozzle to remain a fixed distance from the surface of the part at every XY position, as demonstrated in the supplementary video clip (SI 7, Fig. S8). To validate this process flow,

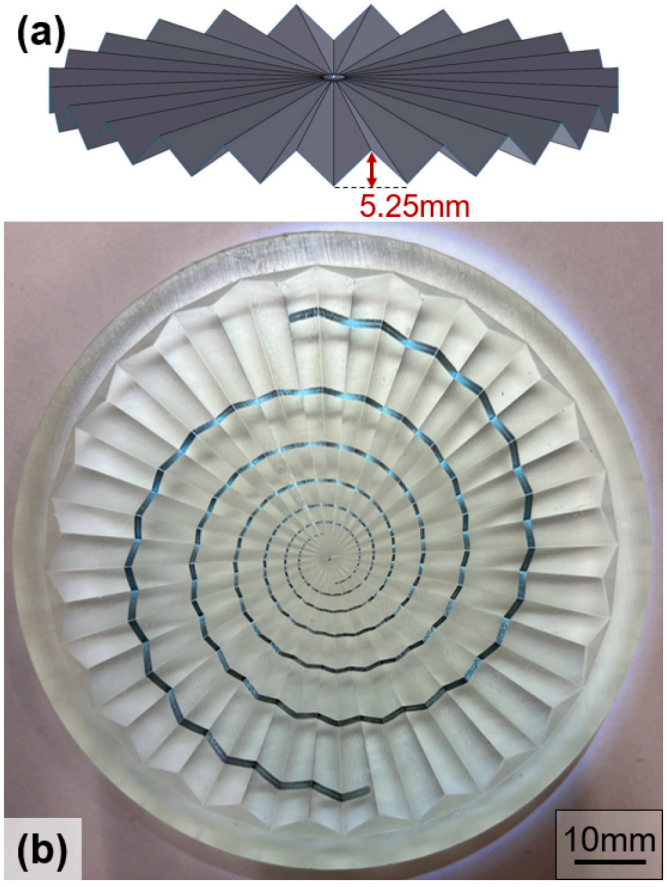

Fig. 9. (a) CAD model of the corrugated disk, having a 45° triangular wave pattern extending 40 mm radially and a maximum height of 5.25 mm at the outer edge. (b) Spiral pattern printed with silver nanoparticle ink via AJP on a substrate fabricated via SLA.

the substrate was fabricated via stereolithography, and the spiral pattern was printed via AJP using the silver nanoparticle ink. The carrier gas flow rate was set to 15 sccm with a focusing ratio of 5, and the Cartesian feed rate relative to the surface of the part was set to 10 mm/s. Visual inspection of the resulting print (Fig. 9b) revealed little variation in line morphology and deposition rate across the sample. In general, this result shows that aerosol jet printing complex patterns onto substrates with an oblique jet geometry up to at least 45° is feasible and can enable complex electronics that would be challenging to produce via other methods.

5. Conclusions

In closing, the asymmetric gas velocity field characteristic of an oblique print orientation influences the impaction physics for AJP. Numerical modeling was applied to understand this process and revealed asymmetry in the cross-section of the printed line, an increase in line width, and a decrease in impaction efficiency. In most cases, this resulted from smaller aerosol droplets more closely following this asymmetric flow field on the downward side of the jet axis. Corresponding models varying the nozzle offset distance also predicted increased line width and decreased impaction efficiency at higher standoff, with interesting results predicted for moderate size particles related to lift force effects. Experiments performed with a custom aerosol jet printer using a 6-axis robot arm as the primary motion system further confirmed that both line morphology and impaction efficiency can be affected by oblique printing. While this study focused primarily on impaction physics, post-deposition liquid-phase spreading is in general a consideration on tilted geometries. Despite this intuition, this mechanism was not observed to impose any limitation in these experiments, and likely mimics constraints for standard horizontal surfaces, suggesting that typical considerations of ink properties, deposition rate, and substrate surface properties apply similarly in the oblique configuration. Rather, neglecting either tilt angle or standoff during the toolpath generation process could lead to localized undesired variations in line width, film thickness, or electrical properties within a print. However, several mitigation strategies are suggested by these results. Increasing carrier or sheath gas flow rates will increase droplet inertia for a given droplet size, minimizing asymmetry and center-shift in the resulting cross-section, as well as increasing its impaction probability in most cases. Likewise, maintaining reasonably low nozzle standoff distance can reduce droplet spreading and susceptibility to lift force effects after exiting the nozzle. In cases for which these nonidealities of oblique deposition can be controlled or accommodated, this configuration provides a broad design space to improve toolpath planning and enable printing on increasingly complex surfaces.

Declaration of competing interest

The authors declare that they have no known competing financial interests or personal relationships that could have appeared to influence the work reported in this paper.

Acknowledgements

The authors would like to thank Faith L. Moss, Samuel J. Schwartz, and Katherine T. Nelson of Iowa State University for contributing to these efforts as part of their undergraduate research experiences. The authors gratefully acknowledge funding support from the National Science Foundation under NSF CMMI-2224303. E.B.S. further acknowledges the Department of Mechanical Engineering at Iowa State University for access to characterization and computational facilities.

Funding

NSF CMMI-2224303.

Appendix A. Supplementary data

Supplementary data to this article can be found online at https://doi.org/10.1016/j.jmapro.2024.05.004.

References

[1] Vafadar A, Guzzomi F, Rassau A, Hayward K. Advances in metal additive manufacturing: a review of common processes, industrial applications, and current challenges. Appl Sci 2021;11:1213. https://doi.org/10.3390/app11031213.
[2] Yuan S, Shen F, Chua CK, Zhou K. Polymeric composites for powder-based additive manufacturing: materials and applications. Prog Polym Sci 2019;91:141–68. https://doi.org/10.1016/j.progpolymsci.2018.11.001.
[3] Espalin D, Muse DW, MacDonald E, Wicker RB. 3D printing multifunctionality: structures with electronics. Int J Adv Manuf Technol 2014;72:963–78. https://doi.org/10.1007/s00170-014-5717-7.
[4] Hong F, Lampret B, Myant C, Hodges S, Boyle D. 5-axis multi-material 3D printing of curved electrical traces. Addit Manuf 2023;70:103546. https://doi.org/10.1016/j.addma.2023.103546.
[5] Khan Y, Thielens A, Muin S, Ting J, Baumbauer C, Arias AC. A new frontier of printed electronics: flexible hybrid electronics. Adv Mater 2020;32:1905279. https://doi.org/10.1002/adma.201905279.
[6] Khan Y, Garg M, Gui Q, Schadt M, Gaikwad A, Han D, et al. Flexible hybrid electronics: direct interfacing of soft and hard electronics for wearable health monitoring. Adv Funct Mater 2016;26:8764–75. https://doi.org/10.1002/adfm.201603763.
[7] Lim H, Kim HS, Qazi R, Kwon Y, Jeong J, Yeo W. Advanced soft materials, sensor integrations, and applications of wearable flexible hybrid electronics in healthcare, energy, and environment. Adv Mater 2020;32:1901924. https://doi.org/10.1002/adma.201901924.
[8] Paulsen JA, Renn M, Christenson K, Plourde R. Printing conformal electronics on 3D structures with Aerosol Jet technology. In: 2012 future instrum. int. workshop FIIW proc., IEEE, Gatlinburg, TN, USA; 2012. p. 1–4. https://doi.org/10.1109/FIIW.2012.6378343.

[9] Konstantinou X, Albrecht JD, Chahal P, Papapolymerou J. Flexible chip-first millimeter-wave packaging using multiple dielectrics. IEEE Trans Compon Packag Manuf Technol 2022;12:682–91. https://doi.org/10.1109/TCPMT.2022.3160626.
[10] Konstantinou X, Sturim N, Albrecht JD, Chahal P, Papapolymerou J. A power-efficient compact Ku-band system-on-antenna module with chip-first package integration. In: 2023 IEEE radio wirel. symp. RWS, IEEE, Las Vegas, NV, USA; 2023. p. 125–8. https://doi.org/10.1109/RWS55624.2023.10046346.
[11] Rosker ES, Barako MT, Nguyen E, DiMarzio D, Kisslinger K, Duan D-W, et al. Approaching the practical conductivity limits of aerosol jet printed silver. ACS Appl Mater Interfaces 2020;12:29684–91. https://doi.org/10.1021/acsami.0c06959.
[12] Wang C, Hong G-Y, Li K-M, Young H-T. A miniaturized nickel oxide thermistor via aerosol jet technology. Sensors 2017;17:2602. https://doi.org/10.3390/s17112602.
[13] Eckstein R, Rödlmeier T, Glaser T, Valouch S, Mauer R, Lemmer U, et al. Aerosol-jet printed flexible organic photodiodes: semi-transparent, color neutral, and highly efficient. Adv Electron Mater 2015;1:1500101. https://doi.org/10.1002/aelm.201500101.
[14] Parate K, Rangnekar SV, Jing D, Mendivelso-Perez DL, Ding S, Secor EB, et al. Aerosol-jet-printed graphene immunosensor for label-free cytokine monitoring in serum. ACS Appl Mater Interfaces 2020;12:8592–603. https://doi.org/10.1021/acsami.9b22183.
[15] Cao C, Andrews JB, Franklin AD. Completely printed, flexible, stable, and hysteresis-free carbon nanotube thin-film transistors via aerosol jet printing. Adv Electron Mater 2017;3:1700057. https://doi.org/10.1002/aelm.201700057.
[16] Lu S, Cardenas JA, Worsley R, Williams NX, Andrews JB, Casiraghi C, et al. Flexible, print-in-place 1D–2D thin-film transistors using aerosol jet printing. ACS Nano 2019;13:11263–72. https://doi.org/10.1021/acsnano.9b04337.
[17] Deiner LJ, Jenkins T, Howell T, Rottmayer M. Aerosol jet printed polymer composite electrolytes for solid-state Li-ion batteries. Adv Eng Mater 2019;21:1900952. https://doi.org/10.1002/adem.201900952.
[18] Deiner LJ, Jenkins T, Powell A, Howell T, Rottmayer M. High capacity rate capable aerosol jet printed Li-ion battery cathode. Adv Eng Mater 2019;21:1801281. https://doi.org/10.1002/adem.201801281.
[19] Stoukatch S, Laurent P, Dricot S, Axisa F, Seronveaux L, Vandormael D, et al. Evaluation of Aerosol Jet Printing (AJP) technology for electronic packaging and interconnect technique. In: 2012 4th electron. syst.-integr. technol. conf., IEEE, Amsterdam, Netherlands; 2012. p. 1–5. https://doi.org/10.1109/ESTC.2012.6542067.
[20] Seifert T, Baum M, Roscher F, Wiemer M, Gessner T. Aerosol jet printing of nano particle based electrical chip interconnects. Mater Today Proc 2015;2:4262–71. https://doi.org/10.1016/j.matpr.2015.09.012.
[21] Werum K, Mueller E, Keck J, Jaeger J, Horter T, Glaeser K, et al. Aerosol jet printing and interconnection technologies on additive manufactured substrates. J Manuf Mater Process 2022;6:119. https://doi.org/10.3390/jmmp6050119.
[22] Saeidi-Javash M, Kuang W, Dun C, Zhang Y. 3D conformal printing and photonic sintering of high-performance flexible thermoelectric films using 2D nanoplates. Adv Funct Mater 2019;29:1901930. https://doi.org/10.1002/adfm.201901930.
[23] Vella S, Smithson C, Halfyard K, Shen E, Chrétien M. Integrated capacitive sensor devices aerosol jet printed on 3D objects. Flex Print Electron 2019;4:045005. https://doi.org/10.1088/2058-8585/ab59c0.
[24] Rosker ES, Barako MT, Nguyen E, Radisic V, Goorsky MS, Tice J. Fully 3D printed high performance band-stop filters enabled by three-dimensional design. Flex Print Electron 2022;7:035006. https://doi.org/10.1088/2058-8585/ac825a.
[25] Goh GL, Dikshit V, Koneru R, Peh ZK, Lu W, Goh GD, et al. Fabrication of design-optimized multifunctional safety cage with conformal circuits for drone using hybrid 3D printing technology. Int J Adv Manuf Technol 2022;120:2573–86. https://doi.org/10.1007/s00170-022-08831-y.
[26] Flagan RC, Seinfeld JH. Fundamentals of air pollution engineering. Englewood Cliffs, NJ: Prentice Hall; 1988. p. 542.
[27] Ramesh S, Xu Z, Rivero IV, Cormier DR. Computational fluid dynamics and experimental validation of aerosol jet printing with multi-stage flow focusing lenses. J Manuf Process 2023;95:312–29. https://doi.org/10.1016/j.jmapro.2023.03.035.
[28] Salary R, Lombardi JP, Samie Tootooni M, Donovan R, Rao PK, Borgesen P, et al. Computational fluid dynamics modeling and online monitoring of aerosol jet printing process. J Manuf Sci Eng 2017;139:021015. https://doi.org/10.1115/1.4034591.
[29] Chen G, Gu Y, Tsang H, Hines DR, Das S. The effect of droplet sizes on overspray in aerosol-jet printing. Adv Eng Mater 2018;20:1701084. https://doi.org/10.1002/adem.201701084.
[30] Salary R (Ross), Lombardi JP, Weerawarne DL, Rao P, Poliks MD. A computational fluid dynamics investigation of pneumatic atomization, aerosol transport, and deposition in aerosol jet printing process. J Micro Nano-Manuf 2021;9:010903. https://doi.org/10.1115/1.4049958.
[31] Feng JQ, Ramm A, Renn MJ. A quantitative analysis of overspray in Aerosol Jet® printing. Flex Print Electron 2021;6:045006. https://doi.org/10.1088/2058-8585/ac3019.
[32] Gamba L, Johnson ZT, Atterberg J, Diaz-Arauzo S, Downing JR, Claussen JC, et al. Systematic design of a graphene ink formulation for aerosol jet printing. ACS Appl Mater Interfaces 2023;15:3325–35. https://doi.org/10.1021/acsami.2c18838.
[33] Feng JQ, Renn MJ. Aerosol Jet® direct-write for microscale additive manufacturing. J Micro Nano-Manuf 2019;7:011004. https://doi.org/10.1115/1.4043595.
[34] Lozano A, Garcia JA, Navarro JL, Calvo E, Barreras F. Influence of viscosity on droplet size distribution and generation rate in ultrasonic atomization. At Sprays 2010;20:923–34. https://doi.org/10.1615/AtomizSpr.v20.i11.10.
[35] Donnelly TD, Hogan J, Mugler A, Schubmehl M, Schommer N, Bernoff AJ, et al. Using ultrasonic atomization to produce an aerosol of micron-scale particles. Rev Sci Instrum 2005;76:113301. https://doi.org/10.1063/1.2130336.
[36] Secor EB. Guided ink and process design for aerosol jet printing based on annular drying effects. Flex Print Electron 2018;3:035007. https://doi.org/10.1088/2058-8585/aadffd.
[37] Tafoya RR, Secor EB. Understanding effects of printhead geometry in aerosol jet printing. Flex Print Electron 2020;5:035004. https://doi.org/10.1088/2058-8585/aba2bb.
[38] Feng JQ. Mist flow visualization for round jets in Aerosol Jet ® printing. Aerosol Sci Tech 2019;53:45–52. https://doi.org/10.1080/02786826.2018.1532566.
[39] Akhatov IS, Hoey JM, Swenson OF, Schulz DL. Aerosol focusing in micro-capillaries: theory and experiment. J Aerosol Sci 2008;39:691–709. https://doi.org/10.1016/j.jaerosci.2008.04.004.
[40] Akhatov IS, Hoey JM, Swenson OF, Schulz DL. Aerosol flow through a long micro-capillary: collimated aerosol beam. Microfluid Nanofluidics 2008;5:215–24. https://doi.org/10.1007/s10404-007-0239-3.